Supplementary Information

Revealing the nano-scale mechanisms of the limited non-basal plasticity in magnesium

Jiwon Jeong[1,†], Zhuocheng Xie[2,†], Markus Alfreider[3], Sandra Korte-Kerzel[2], Daniel Kiener[3], Julien Guénolé[4,*], Sang Ho Oh[5*]

[1] Department of Structure and Nano-/Micromechanics of Materials, Max-Planck Institut für Eisenforschung GmbH, Düsseldorf, 40237, Germany
[2] Institute of Physical Metallurgy and Materials Physics, RWTH Aachen University, 52056 Aachen, Germany
[3] Department of Materials Science, Montanuniversität Leoben, Jahnstraße 12, 8700 Leoben, Austria
[4] Université de Lorraine, CNRS, Arts et Métiers ParisTech, LEM3, Metz, 57070, France
[5] Department of Energy Engineering, KENTECH Institute for Energy Materials and Devices, Korea Institute of Energy Technology (KENTECH), Naju 58330, Republic of Korea.

†These authors contributed equally

*Corresponding authors: shoh@kentech.ac.kr, julien.guenole@cnrs.fr

Table of Contents

1 Material and methods: extended description

1.1 Sample preparation

A cylindrical bar of Mg single crystal with a purity of 99.999% was purchased from Goodfellow (Goodfellow Cambridge Ltd). The length direction of the bar was parallel to the [0001] direction, with an orientation accuracy of < 2%. A side plane of the bar was cut parallel to the $\{11\bar{2}0\}$ plane to indicate the in-plane orientation. The bar was further sliced to obtain the desired orientations [0001] and $[2\bar{1}\bar{1}2]$ using a wire saw (Well 3232). For the mechanical polishing of the sliced specimen, alcohol-based diamond suspension was used to avoid rapid oxidation. The final polishing was conducted using 0.25 µm diamond suspension. For an exact determination of the crystal orientation, electron backscatter diffraction (EBSD) scans were applied, showing that the angular mismatch between desired and actual orientation is 7 ± 2°. For investigation of the mechanical size effect using mechanical testing in the SEM, cuboid pillars with diameters in the micron to sub-micron range were fabricated using a focused ion beam (FIB) workstation (Leo 1540 XB, Carl Zeiss). Before FIB machining, the bulk sample was thinned and electrolytically etched by immersing it in a solution (5 mL perchloric acid + 95 mL methanol) at -40 ˚C and a potential of 30 V. This process removes large areas of material and minimizes the FIB working time. The cuboidal pillars were fabricated within a thinned region of wedge sample using a 30 kV Ga^+ ion beam. The size of the specimens was fixed as 0.5, 1, 2, and 4 µm. Applied ion currents were ranging from 5 nA for coarse cuts to 10 pA for final polishing of the pillar surface. The pillars had aspect ratios of ~1:3, which is appropriate to micro-compression tests. To investigate the deformation mechanism of Mg using in-situ TEM, pillars were fabricated using again a focused ion beam workstation (FIB, Helios NanoLab 450S, FEI). Before the FIB process, the working area was carefully selected because deformation twins were induced at the surface of polished sample during mechanical polishing process. Therefore, to ensure single crystallinity of the pillars, the working area for FIB machining was selected apart from twinned regions. The thin foil was prepared from the surface of the bulk Mg sample by cross-sectional milling. This thin foil was attached to a Cu grid by Pt deposition. Coarse micropillars were fabricated within the thin foil using a beam current of 93 pA at 30 kV in an annular milling mode. To avoid redeposition problems, all pillars were machined at once using parallel milling mode. Subsequently, fine milling of the pillars with 48 pA ion current was conducted to obtain the cylindrical shaped of the pillars with a diameter of 500 nm. Subsequent low energy millings with 5 kV and 1 kV followed to reduce the surface damage layer. Annealing was performed to remove the final defects at the surface damage layer of the pillar. When the temperature is increased high enough to allow for vacancy diffusion, the edge of pillar can be rounded and oxidized. In Mg, it was shown that defects generated by Ga^+ ion irradiation were annihilated when the temperature is increased from room temperature to half the melting temperature (~160 ˚C) for30 minutes.

1.2 In-situ SEM experiments

Micro-compression tests were performed in-situ in a field emission SEM (LEO 982, Carl Zeiss) using two different setups, due to the large range of pillar sizes and a frame grabbing system for a later correlation of images with mechanical data. The larger pillars (2 µm and 4 µm) were tested using a microindenter system (UNAT-SEM 1, ASMEC) with a maximum applicable force of 300 mN and a conductive conical tungsten tip with a diameter of 16 µm. Due to the lower forces and displacements needed for the smaller pillars (500 nm and 1 µm), better resolution in these parameters was necessary for the same validity of measured data. Therefore, a picoindenter system (PI-85, Hysitron) with a maximum force of 10 mN and a flat ended conductive diamond cube-corner shaped tip with an edge length of 7 µm (Synton MDP, Nidau, Switzerland) was used.

1.3 In-situ TEM experiments

In-situ compression tests were conducted for annealed pillars using a nanoindentation TEM holder (TEM-indenter, Nanofactory) equipped with a diamond punch tip. The compression test was carried out in displacement-controlled mode. To record the deformation behavior of the pillars during the compression test, real-time TEM movies were captured using a charge coupled device camera (ORIUS 200D, Gatan) at 25 frames per second.

2 Supplementary table and figures

Table S1. Summary of slip systems and their Schmid factors (SF) under [0001] and [$2\bar{1}\bar{1}2$] axis compression.

Slip system	SF [0001]-axis compression	SF [$2\bar{1}\bar{1}2$]-axis compression
Basal <*a*>	0	0.50
Prismatic <*a*>	0	0
Pyramidal I <*c+a*>	0.40	0.39
Pyramidal II <*c+a*>	0.45	0.30
($01\bar{1}1$)[$0\bar{1}12$] twin	0.42	0.22
($01\bar{1}3$)[$0\bar{3}32$] twin	0.45	0.24

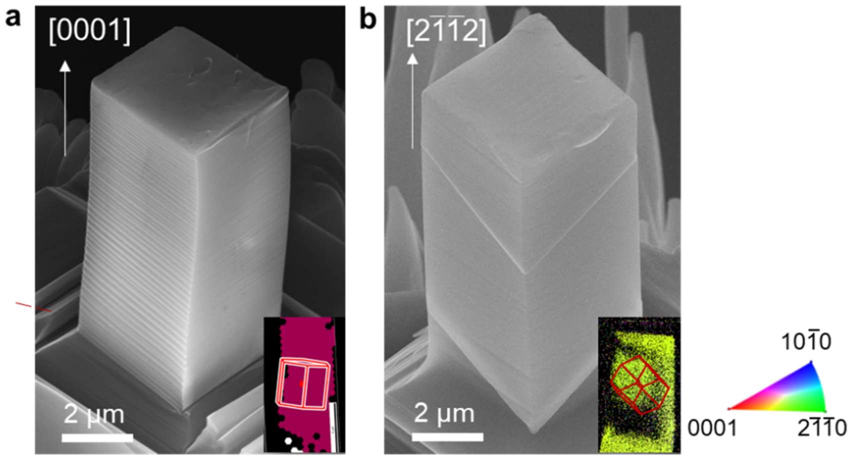

Figure S1. SEM images of (a) c-axis and (b) [$2\bar{1}\bar{1}2$] pillar after micro-compression tests in SEM (refer to Movie S1). The c-axis pillar deformed rather uniformely throughout the pillar axis with exhibiting bending. On the contrary, the defromation of the [$2\bar{1}\bar{1}2$] pillar was strongly localized to a specific slip system with forming pronouncing slip band.

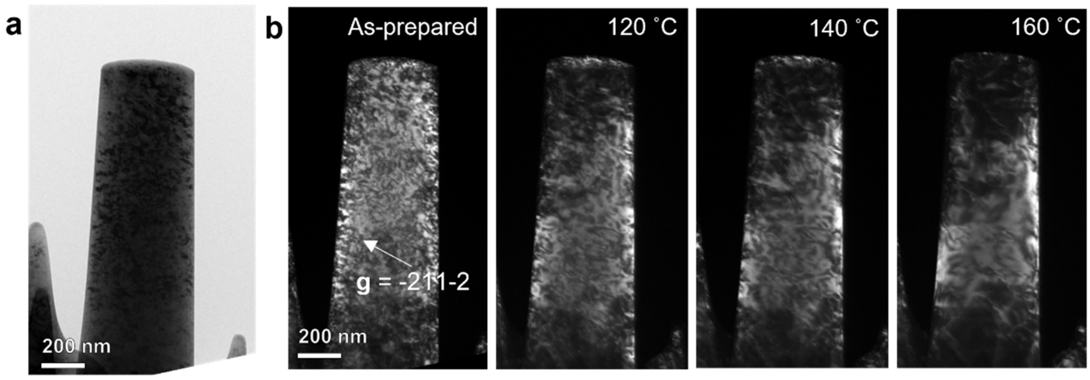

Figure S2. In situ TEM images showing the removal of defects in the Mg pillars induced by FIB. (a) Bright-field TEM image of as-prepared pillar. (b) Dark-field TEM images of as-prepared pillar formed by selecting $(\bar{2}11\bar{2})$ diffraction spot. The TEM images obtained at different temperatures (120, 140 and 160 °C) show the removal FIB-induced defects. After the annealing at 160 °C, the dislocation density was measured to be in the order of ~10^{13} m^{-2}.

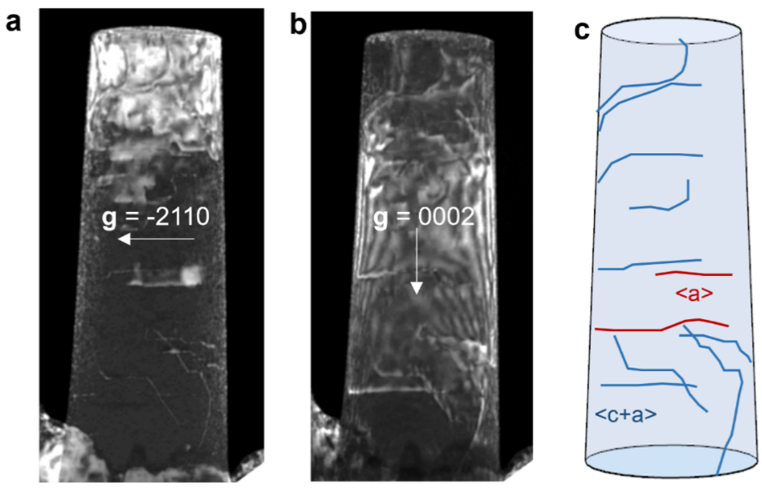

*Figure S1. Dark-field TEM images formed by selcting (a) $(\bar{2}110)$ and (b) (0002) diffraction spot for **g.b** invisibility criterion to determine the Burgers vector of dislocations in the c-axis pillar after annealing in TEM. Most of <c+a> dislocations are visible at the two diffraction conditions but <a> dislocations are invisible when the (0002) diffraction spot is excited (highlighted in red).*

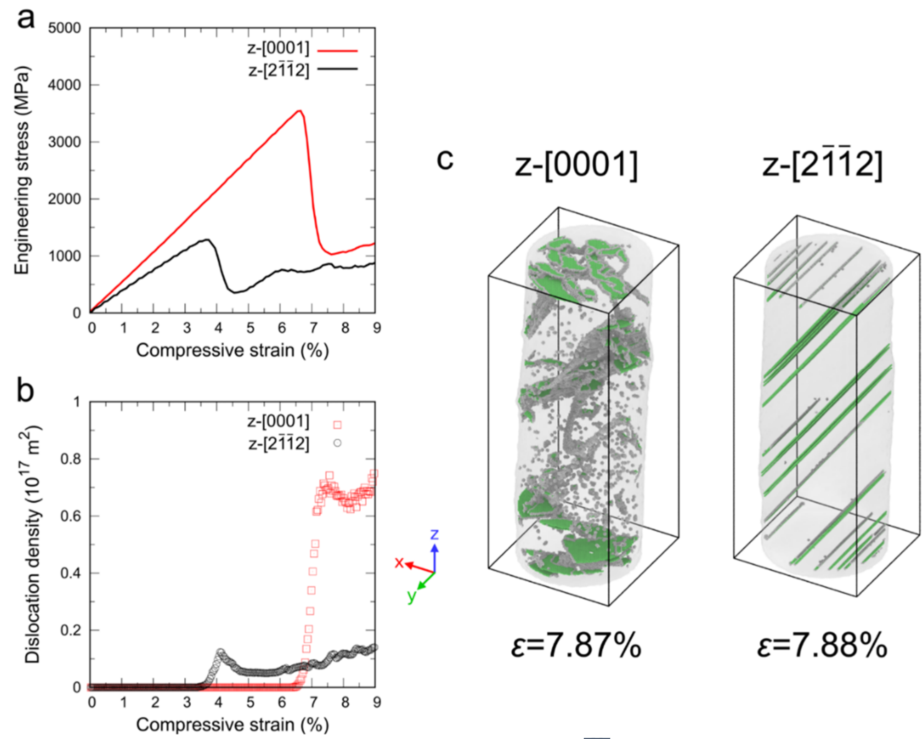

Figure S2. MD simulations of compression tests on [0001] and [2$\bar{1}\bar{1}$2]-oriented Mg nanopillars. The diameter and the length of pillars is 30 nm and 90 nm, respectively. (a) Engineering stress-strain curves. (b) Evolution of dislocation density. (c) Dislocation configuration in the deformed pillars. Colored according to common neighbor analysis, where only atoms in FCC (green) and other (grey) types are shown. Surface meshes are half-transparent. Refer to Movie S4 for the evolution of dislocations with strain.

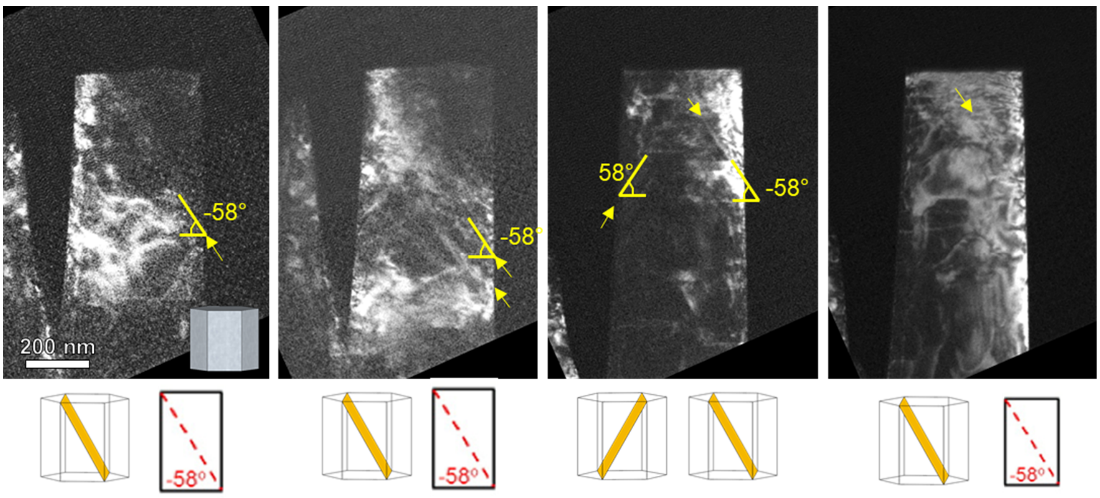

Figure S3. Slip trace analysis of the c-axis pillar under compression. The angle of most of all slip traces measured with respect to the the basal plane is 58°, indicating the <c+a> dislocation slip along the pyramidal II planes.

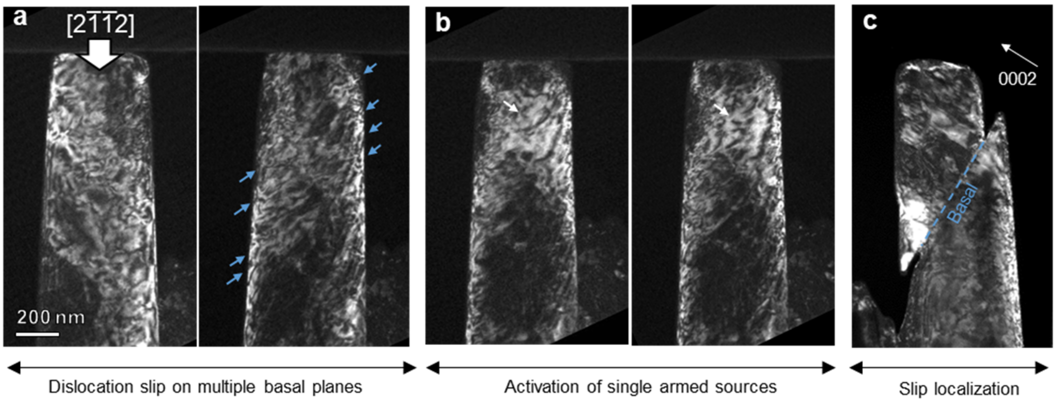

Figure S4. Dark-field TEM images of [2$\bar{1}\bar{1}$2]-oriented pillar showing the evolution of dislocation structure during basal slip. (a) Initial stage of deformation by dislocation slip on multiple basal planes. Blue arrows mark the (0001) slip traces. (b) Activation of single armed source and localization of basal slip. (c) Slip steps formed by localized basal slip.

3 Supplementary movie legends

Movie S1. In-situ SEM micro-compression tests of the *c*-axis and $[2\bar{1}\bar{1}2]$ oriented pillars. The 5 µm pillars were tested using a conductive conical tungsten tip with a diameter of 16 µm.

Movie S2. In-situ TEM compression of the *c*-axis pillar. The cylindrical shaped pillar with the diameter of 500 nm was compressed by using a flat punch under displacement control mode. TEM imaging mode is changed from bright-field to dark-field TEM once the contact between pillar and punch was made and the compression starts. After mobile $\langle c+a \rangle$ dislocations accommodate the initial plasticity of pillars, interactions between dislocations develop local dislocation entanglements. The ensuing plastic strain is accommodated via dislocation avalanches caused by simultaneous activation of multiple dislocation sources, forming a dislocation forest of $\langle c+a \rangle$ dislocations in the confined volume.

Movie S3. In-situ TEM compression of the $[2\bar{1}\bar{1}2]$ oriented pillar. The cylindrical shaped pillar with the diameter of 500 nm was compressed by using a flat punch under displacement control mode. TEM imaging mode is changed from bright-field to dark-field TEM once the contact between pillar and punch was made and the compression starts. The deformation becomes localized with the activation of spiral dislocation sources emitting $\langle a \rangle$ dislocations.

Movie S4. MD simulations of compression tests on [0001] and $[2\bar{1}\bar{1}2]$-oriented Mg nanopillars. The diameter and the length of pillars is 30 nm and 90 nm, respectively. Engineering stress-strain curve is synchronized with the dynamic evolution of dislocation configuration for each pillar. Colored according to common neighbor analysis, where only atoms in FCC (green) and other (grey) types are shown. Surface meshes are half-transparent.